<Supplementary Information>

Efficient Bubble Removal in Superhydrophilic Gas Diffusion Electrodes via Poly(vinyl alcohol) Coating for High-Current Anion-Exchange Membrane Water Electrolysis

In-Ho Baek[a]†, Sang-Mun Jung[a]†, DoEun Kim[b]†, Jihyun Choi[d], Jinwoo Baek[a], Byung-Hun Lee[a], Byung-Jo Lee[a], Haeyong Shin[a], Sang-Hoon You[e], Kyu-Su Kim[f, a], Hyun S. Park[d] *, HangJin Jo[b, c] * and Yong-Tae Kim[a, *]

a : Department of Materials Science and Engineering, Pohang University of Science and Technology, Pohang 37673, Republic of Korea

b : Department of Advanced Nuclear Engineering, Pohang University of Science and Technology, Pohang 37673, Republic of Korea

c : Department of Mechanical Engineering , Pohang University of Science and Technology, Pohang 37673, Republic of Korea

d : Center for Hydrogen-Fuel Cell Research, Korea Institute of Science and Technology (KIST), Seoul 02792, Republic of Korea

e : Department of Mechanical and Automotive Engineering, Kongju National University, Cheonan, 31080, Republic of Korea

f : Department of Mechanical Engineering, Dong-A University (DAU), Busan 49315, Republic of Korea

.

*Corresponding author

Yong-Tae Kim

E-mail: yongtae@postech.ac.kr

Supplementary Text

Figs. S1 to S23

Notes S1 to S5

Tables S1 to S5

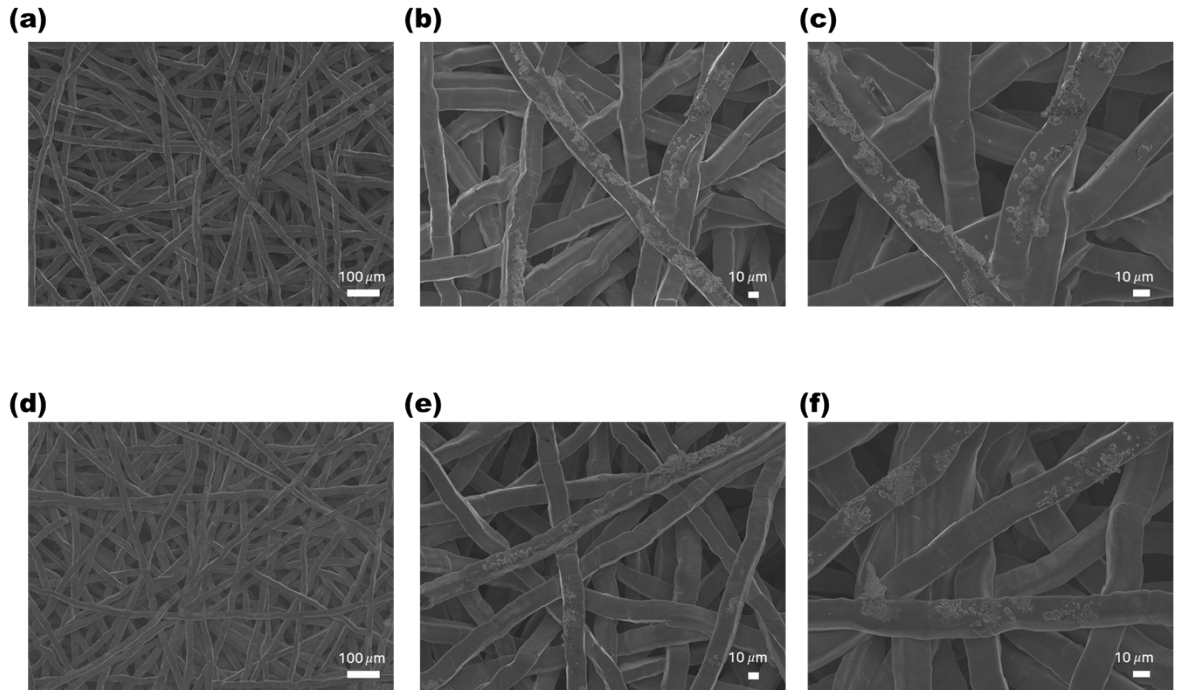

Figure S1. Scanning electron microscopy (SEM) images of the carbon papers (CPs). SEM images of **(a–c)** the bare CP at 100×, 300×, and 500× magnifications, respectively, and **(d–f)** PVA-C0.25 at 100×, 300×, and 500× magnifications, respectively

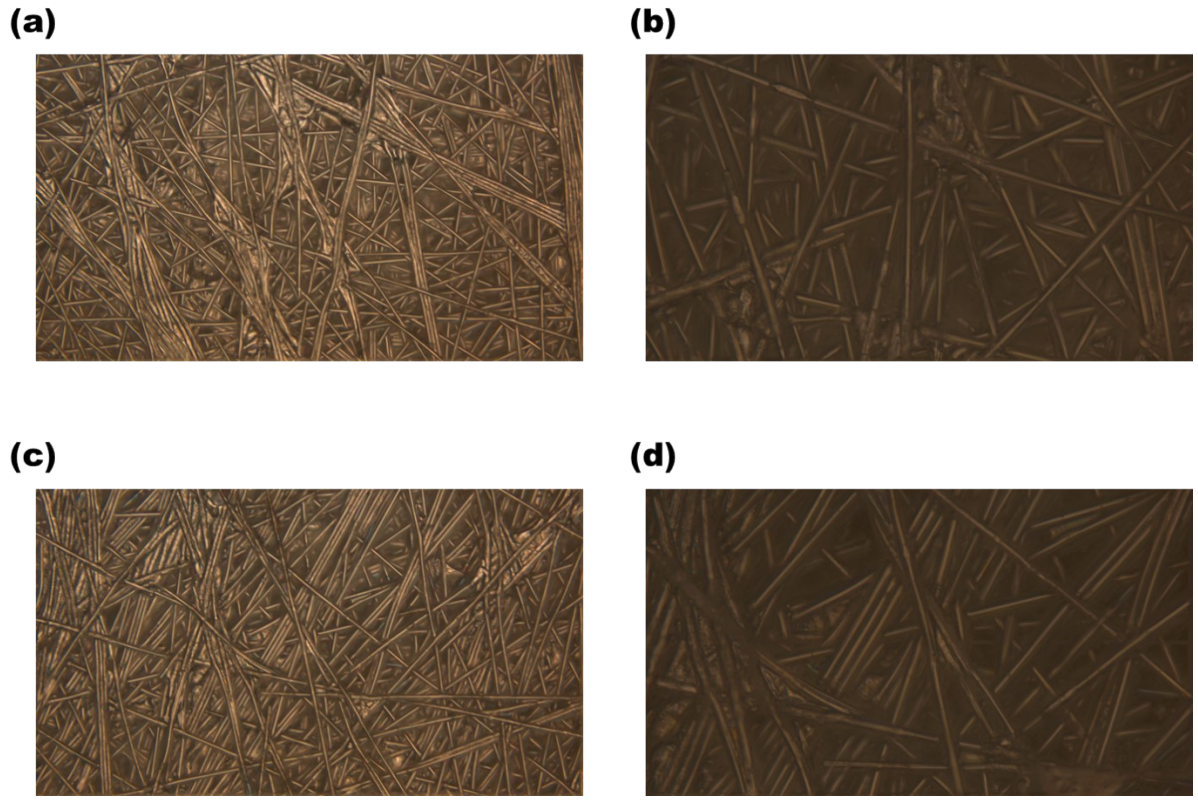

Figure S2. Optical microscopy (OM) images of the CPs. OM images of (a, b) the bare CP and (c, d) PVA-C0.25

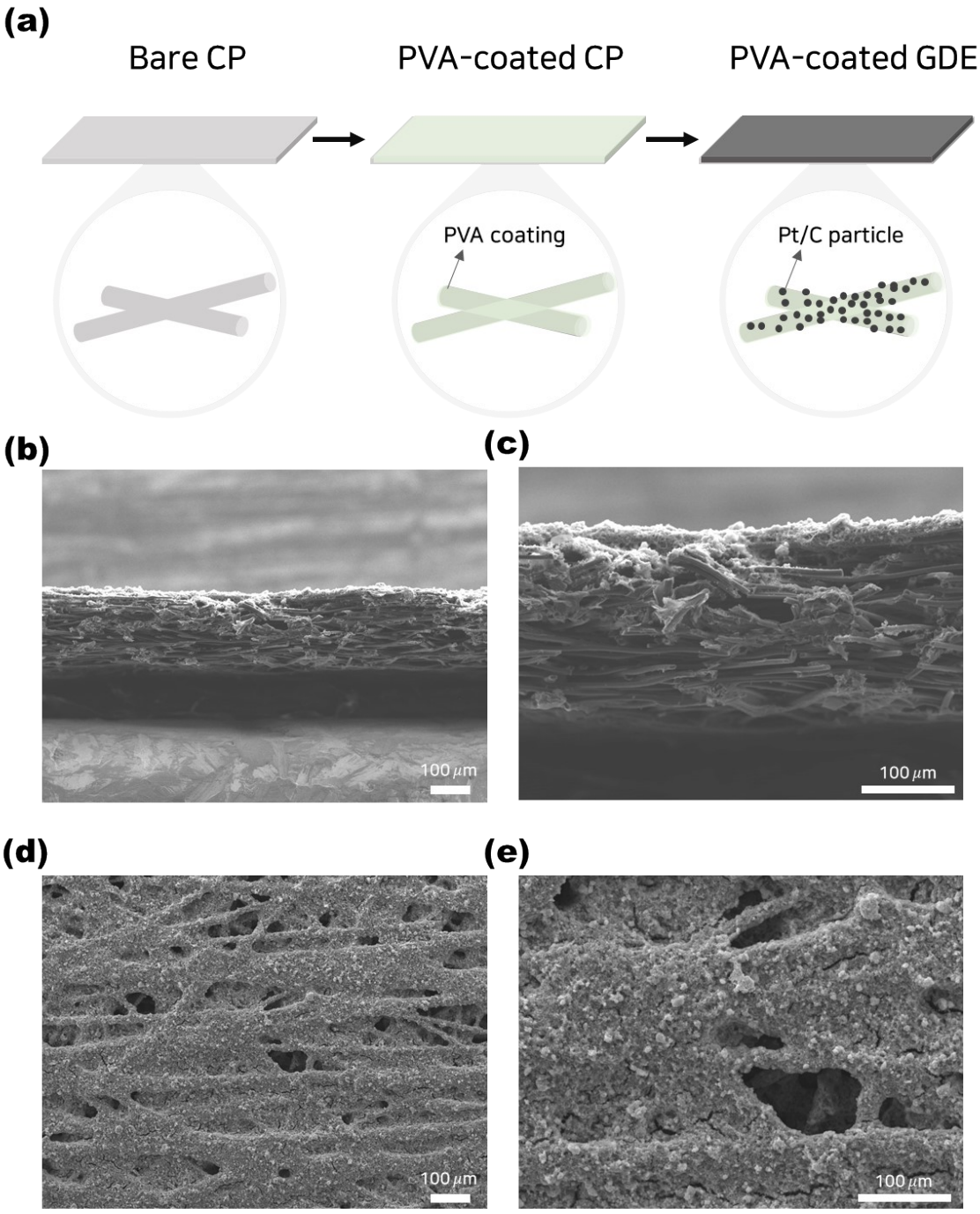

Figure S3. Schematic illustration and scanning electron microscopy (SEM) images of the PVA-coated GDE. (a) Schematic illustration of the sequential fabrication process from bare carbon paper (CP) to PVA-coated CP and finally PVA-coated GDE. (b, c) Cross-sectional SEM images of the PVA-coated GDE at 100× and 250× magnifications, respectively. (d, e) Top-view SEM images of the PVA-coated GDE at 100× and 300× magnifications, respectively.

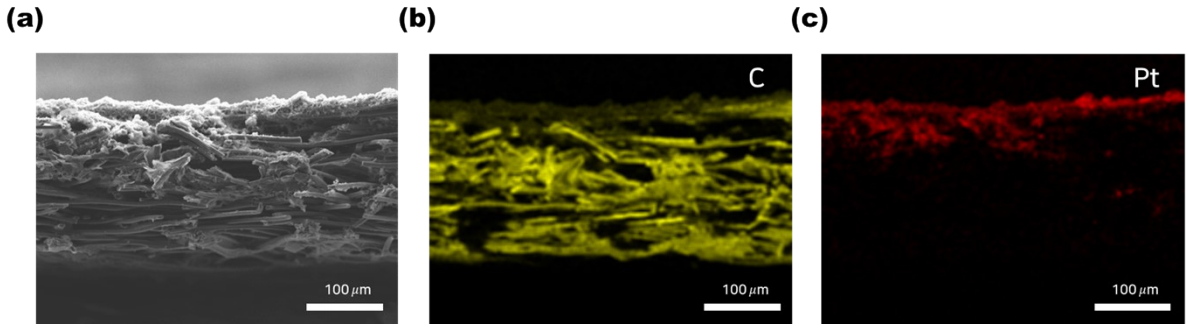

Figure S4. Elemental mapping of the PVA-coated GDE. (a) Cross-sectional SEM image. (b) C elemental map and (c) Pt elemental map, showing the fibrous carbon-paper substrate and the Pt-containing catalyst layer located near the top surface of the electrode.

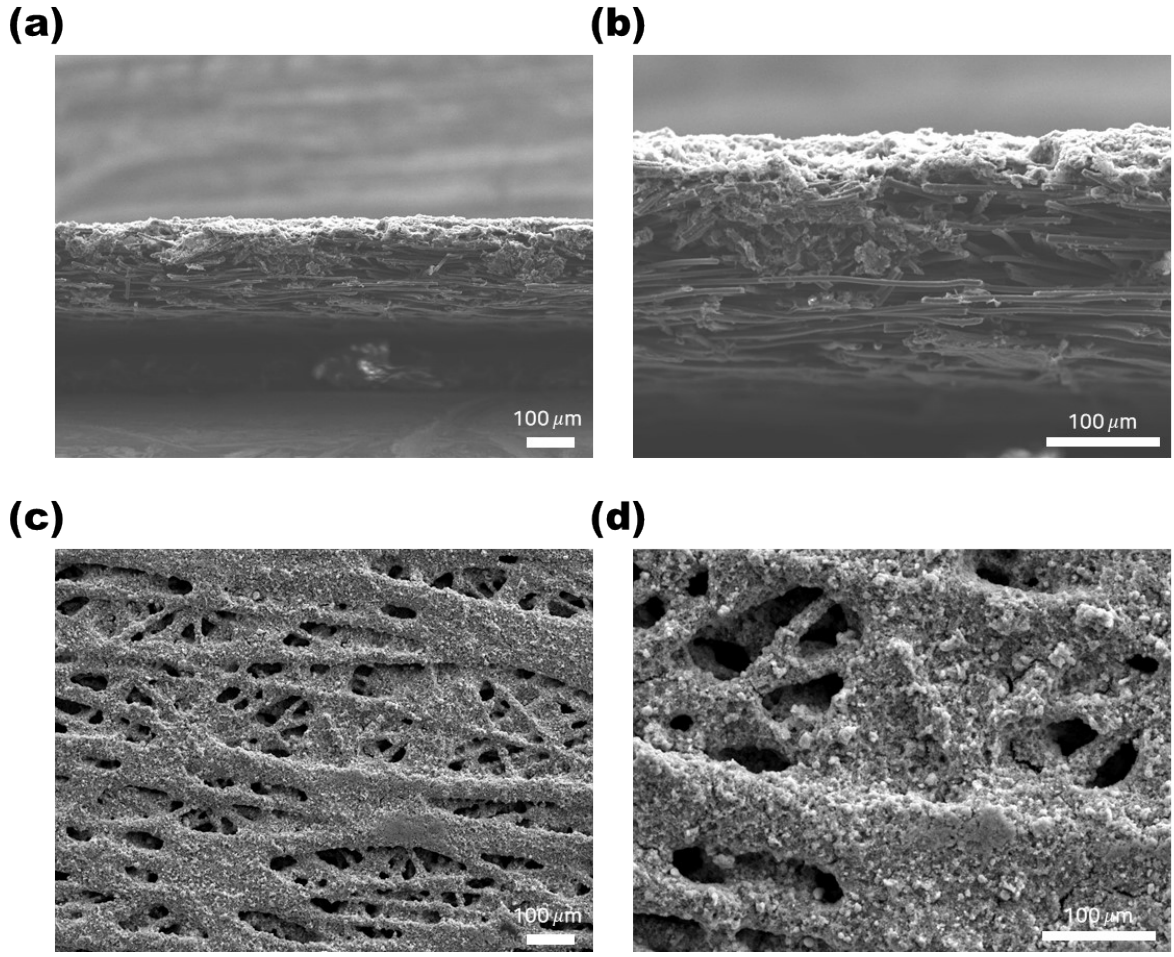

Figure S5. Scanning electron microscopy (SEM) images of the bare CP GDE. (a, b) Cross-sectional SEM images of the bare CP GDE at 100× and 250× magnifications, respectively. (c, d) Top-view SEM images of the bare CP GDE at 100× and 300× magnifications, respectively.

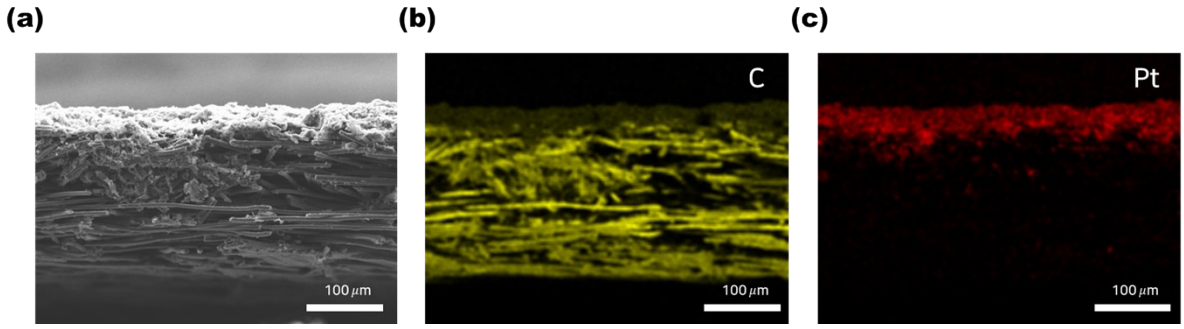

Figure S6. Elemental mapping of the bare CP GDE. (a) Cross-sectional SEM image. (b) C elemental map and (c) Pt elemental map, showing the fibrous carbon-paper substrate and the Pt-containing catalyst layer located near the top surface of the electrode.

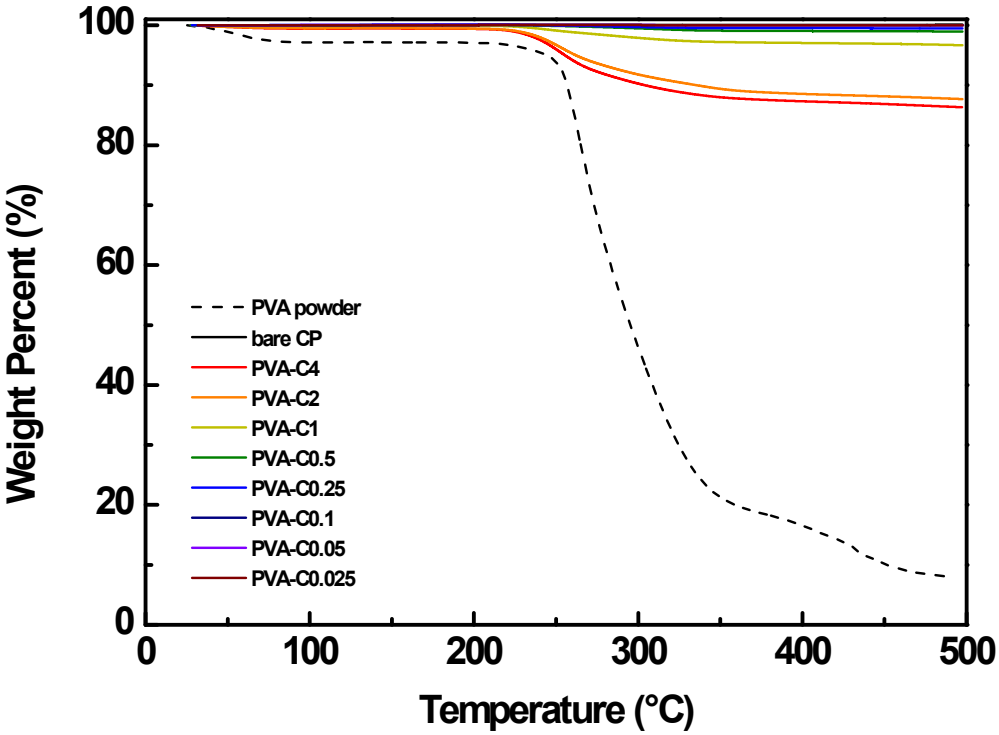

Figure S7. Thermogravimetric analysis (TGA) results of the CPs. TGA thermograms showing the thermal decomposition profiles of the PVA-coated CPs and PVA powder

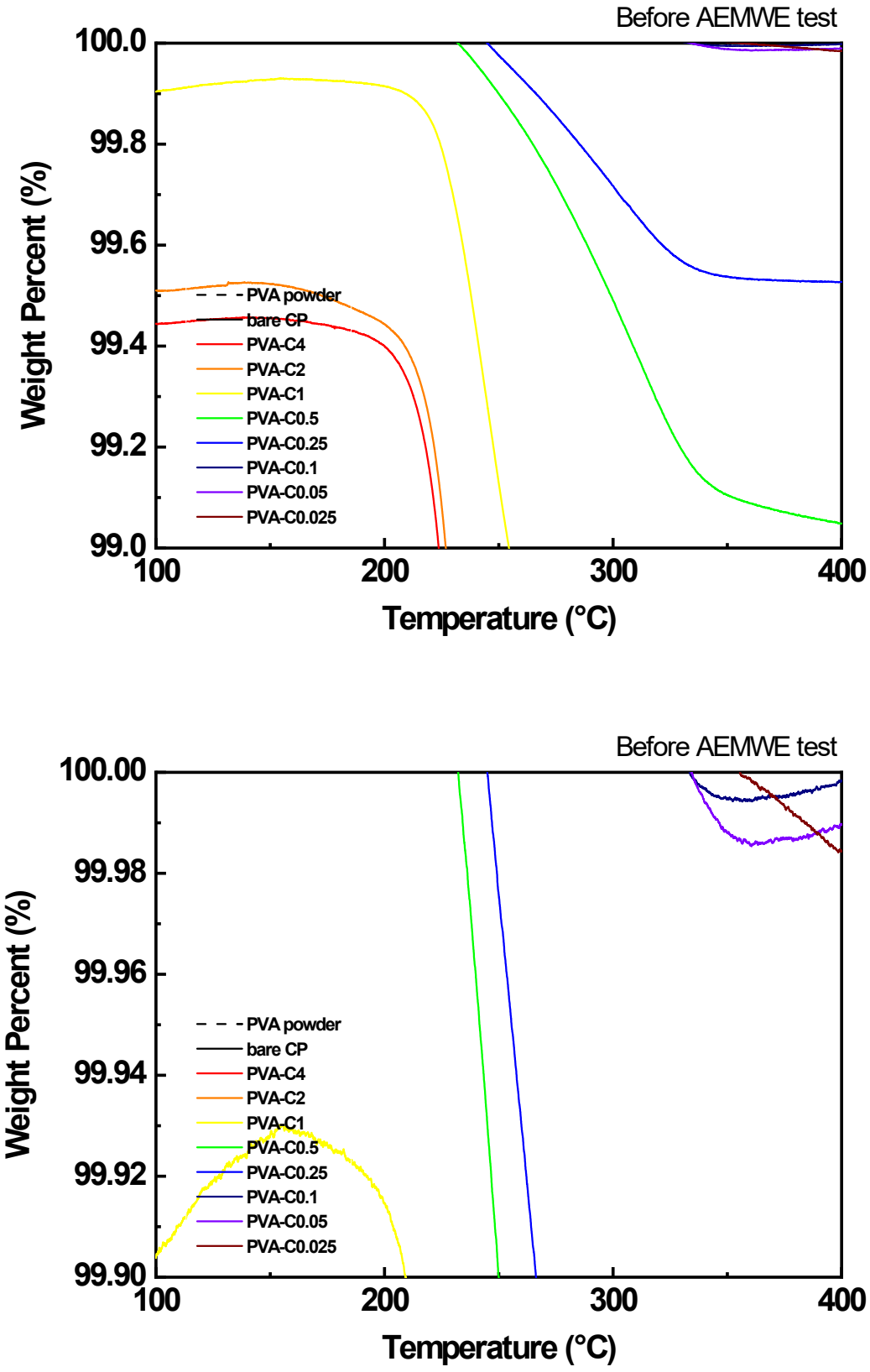

Figure S8. Enlarged view of TGA graph for the PVA-coated CPs.

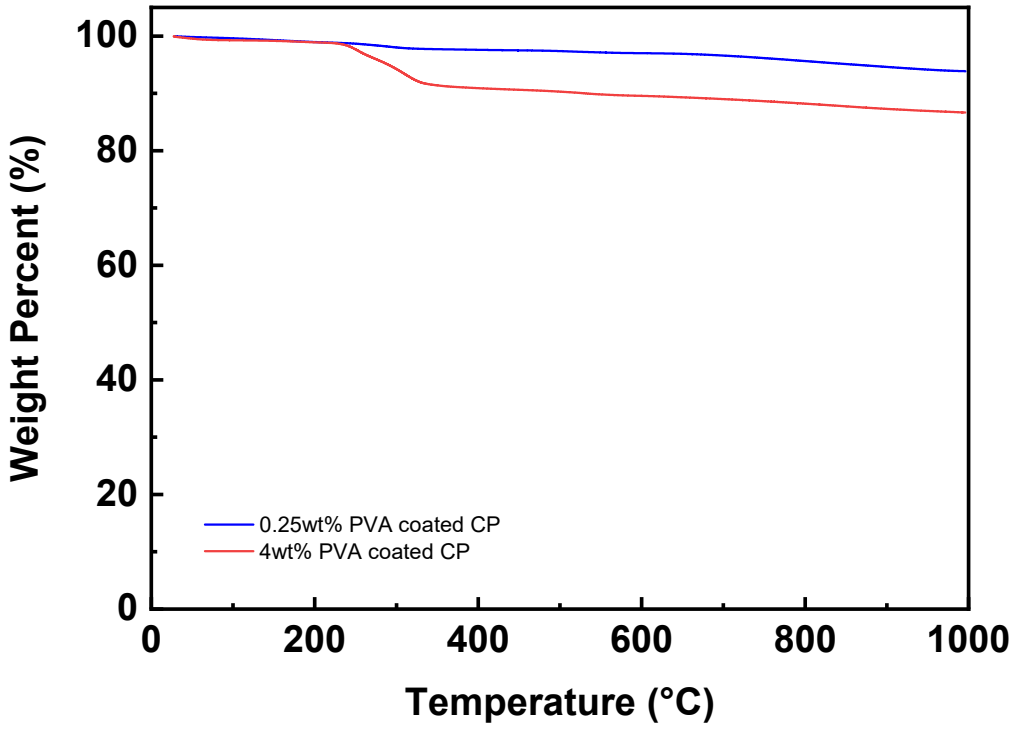

Figure S9. Extended-range TGA graph for the PVA-C0.25 and PVA-C4.

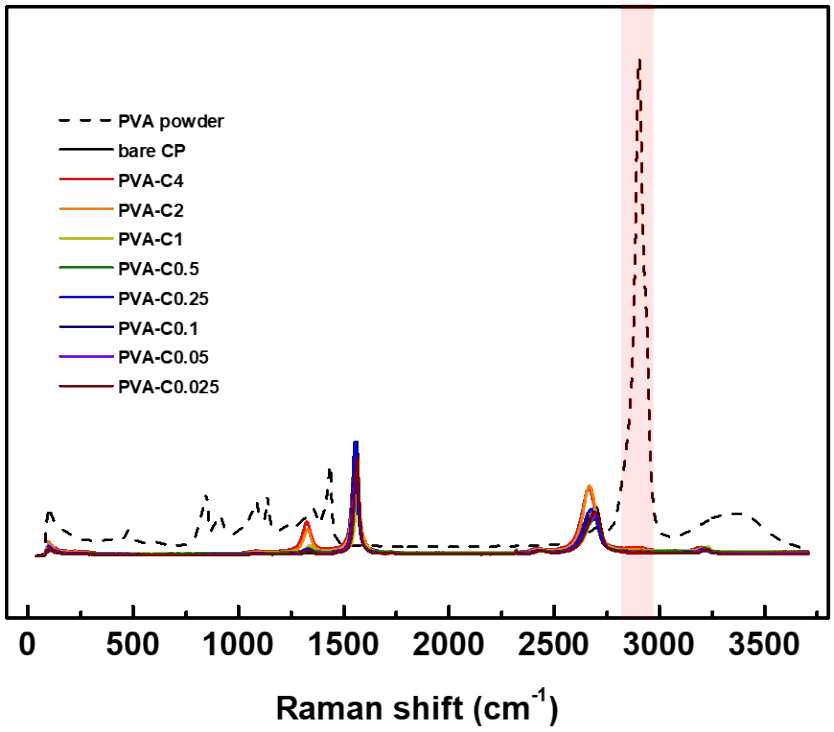

Figure S10. Raman spectra of the CPs. Raman spectra of the PVA-coated CPs and characteristic C–H stretching vibration peak of PVA in the 2900–2950 cm^{-1} range

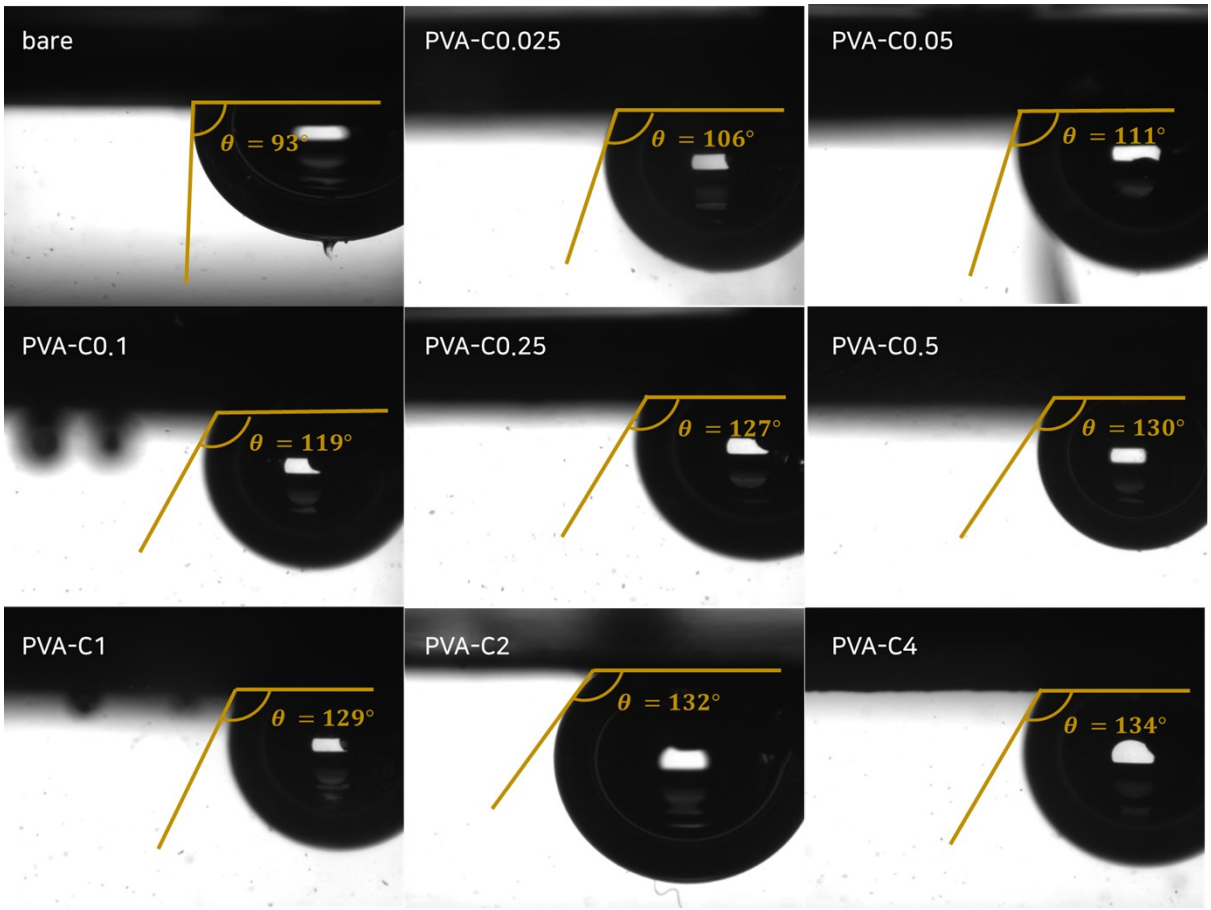

Figure S11. Air bubble contact angles of the CPs. Air bubble contact angles of the PVA-coated CPs and bare CP

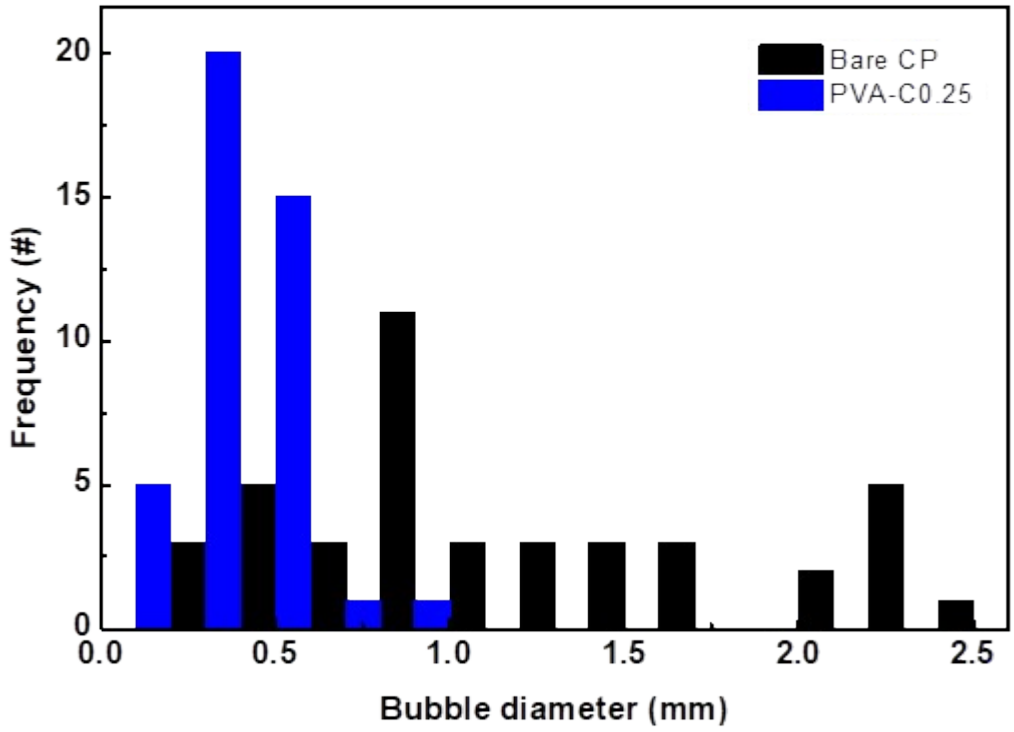

Figure S12. Bubble size distribution histograms. Bubble size distribution histograms for the bare CP and PVA-C0.25

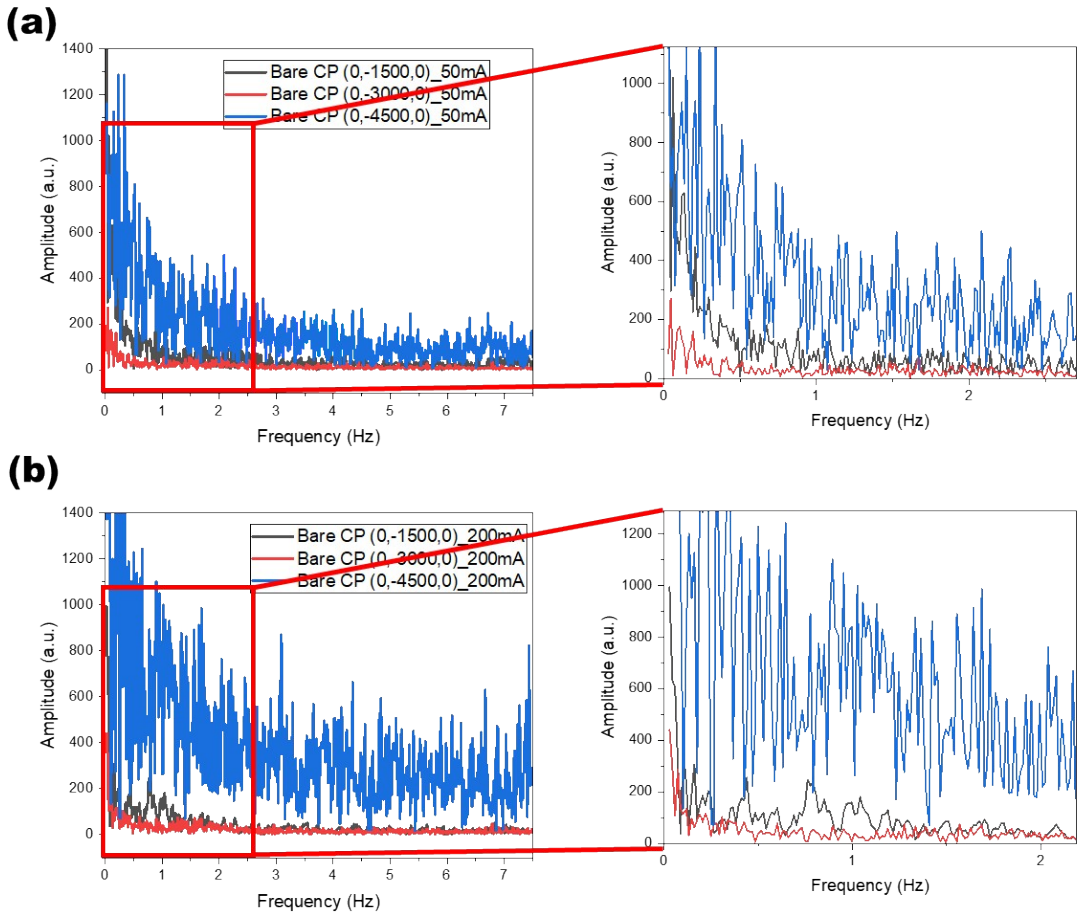

Figure S13. Fast Fourier transform (FFT) analysis of the UME currents for bare CP GDE. SECM measurements were conducted under HER current densities of (a) −50 mA cm^{-2} and (b) −200 mA cm^{-2}.

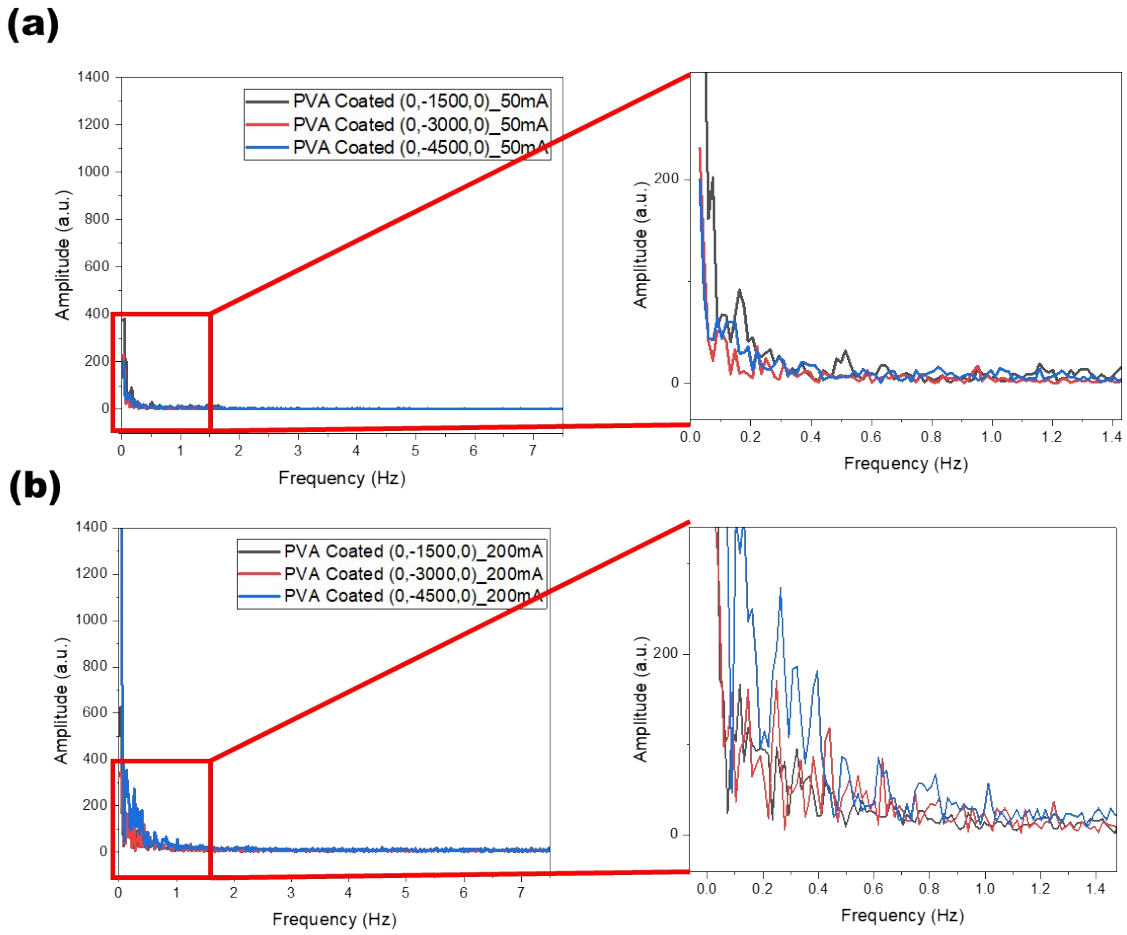

Figure S14. Fast Fourier transform (FFT) analysis of the UME currents for PVA-coated GDE. SECM measurements were conducted under HER current densities of (a) −50 mA cm^{-2} and (b) −200 mA cm^{-2}.

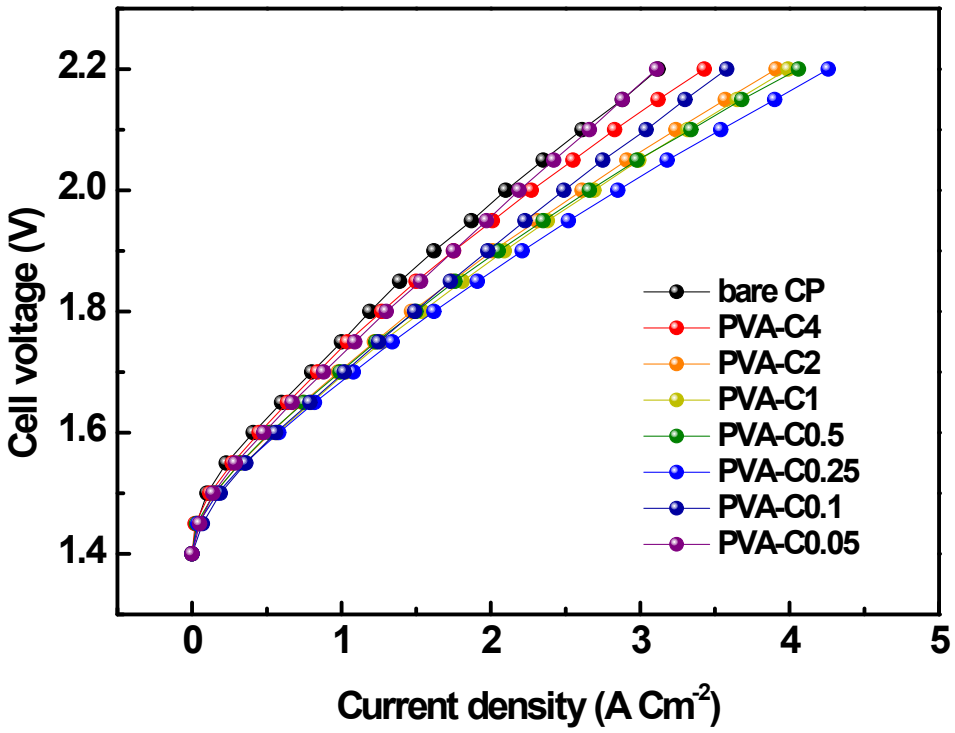

Figure S15. Polarization curves of the AEMWE cells. Polarization curves of the AEMWE cells using the PVA-coated GDEs and bare CP GDE.

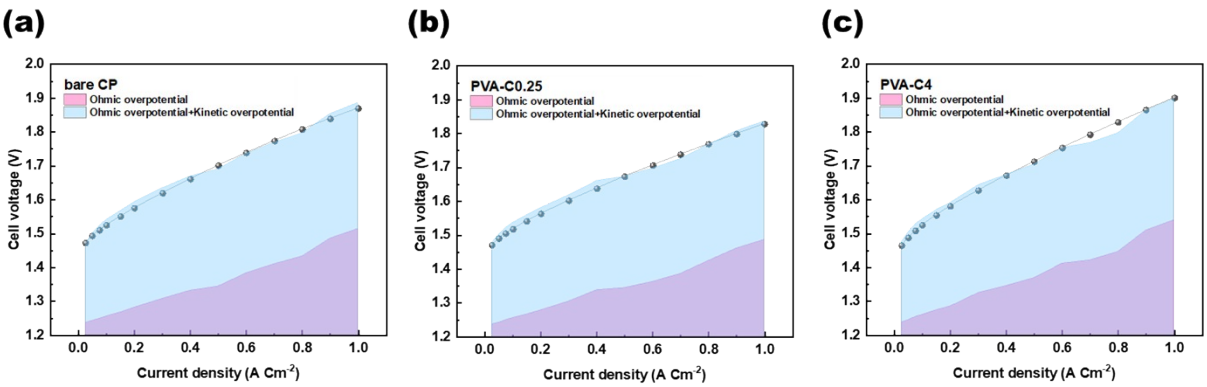

Figure S16. Decoupling overpotentials for the AEMWE cells based on I-V curve. (a) bare CP, (b) PVA-C0.25, (c) PVA-C4

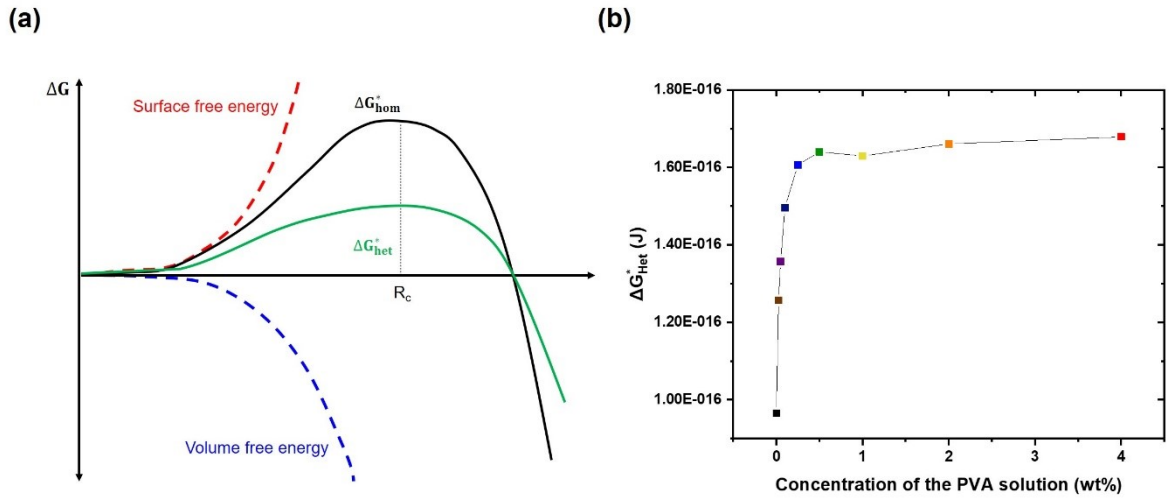

Figure S17. Gibbs free-energy change during nucleation. (a) Schematic illustration of the homogeneous and heterogeneous nucleation models showing the relationship between surface and volume free energy. (b) Variation of the heterogeneous nucleation energy barrier (ΔG^*_{het}) with the PVA coating concentration at a cell voltage of 2 V.

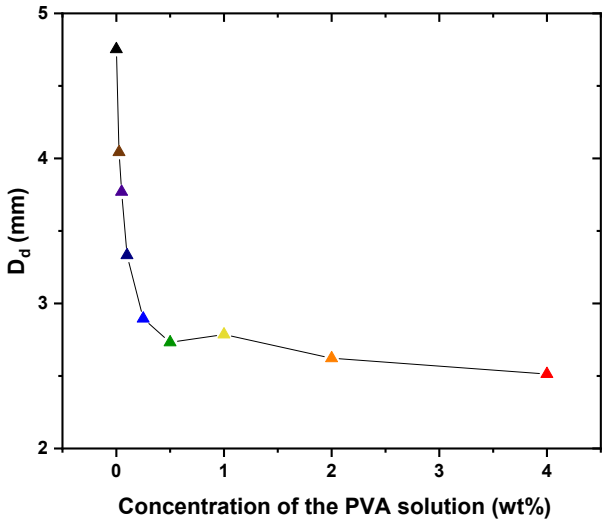

Figure S18. Bubble detachment diameter. Variation in bubble departure diameter (D_d) with the concentration of the PVA coating solution.

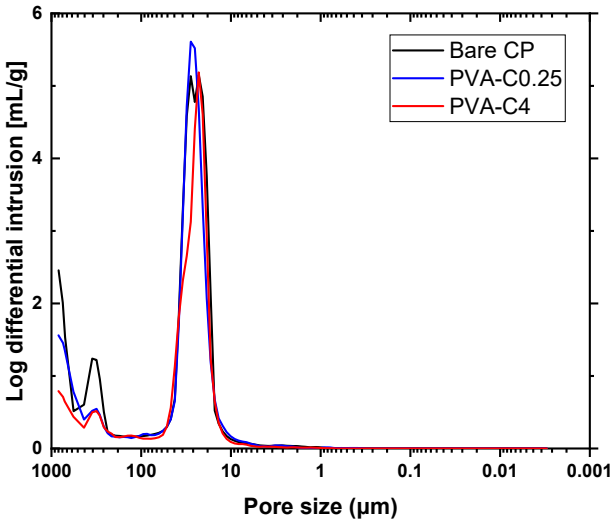

Figure S19. Mercury intrusion porosimetry results as a function of PVA coating concentration. Mercury intrusion porosimetry results for the Bare CP, PVA-C0.25, and PVA-C4 samples.

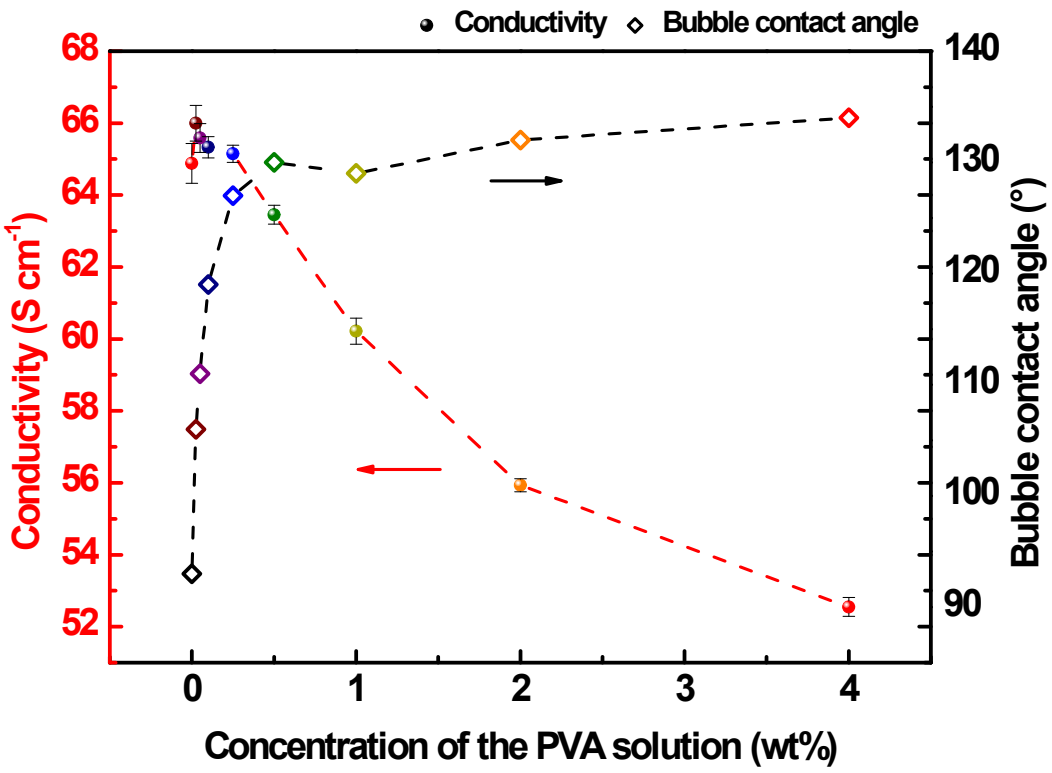

Figure S20. Electrical conductivity with bubble contact angle. Correlation between conductivity and bubble contact angle at various PVA solution concentrations.

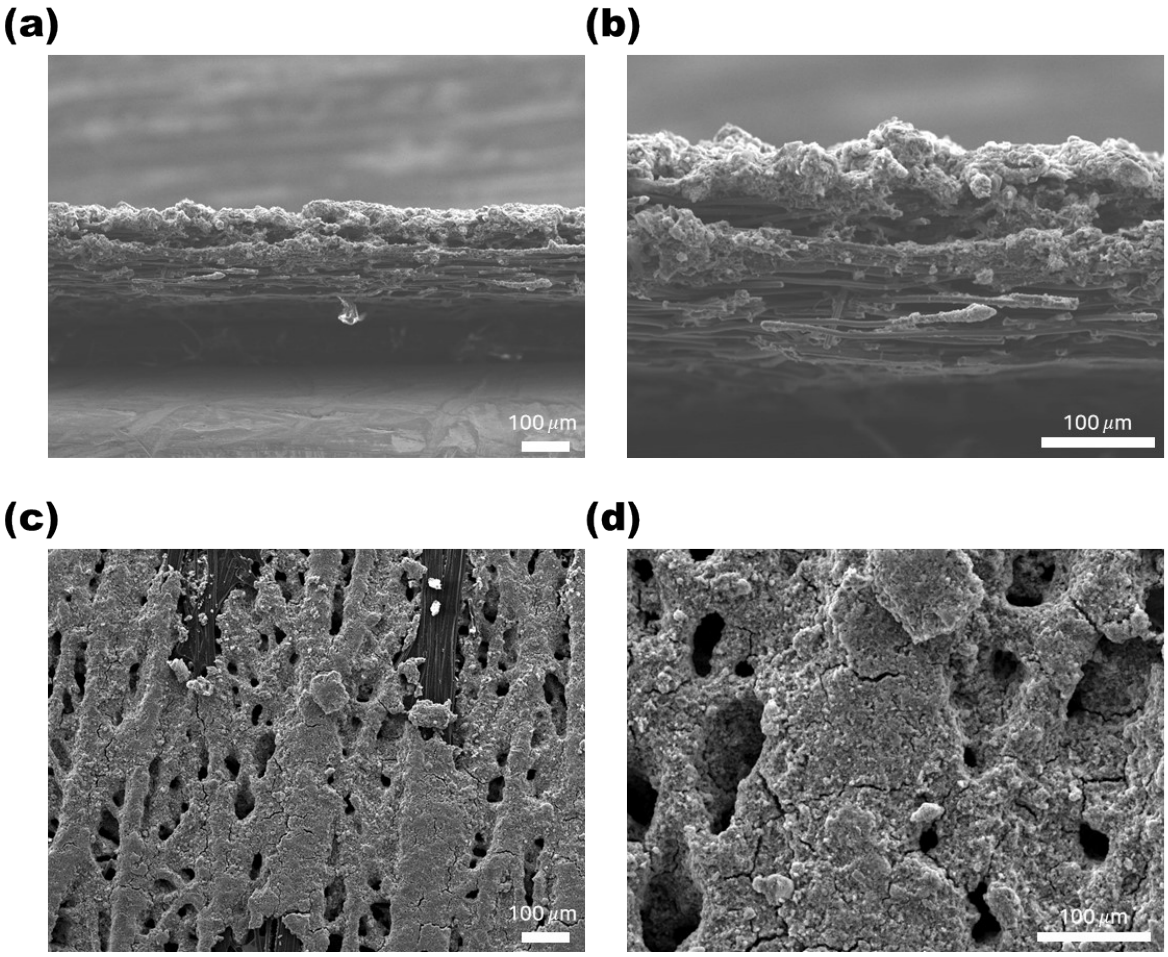

Figure S21. Scanning electron microscopy (SEM) images of the PVA-coated GDE after the AEMWE durability test. SEM images of the (a, b) cross-sections of the PVA-coated GDE after long-term operation at 100× and 250× magnifications, respectively, and (c, d) the corresponding top-view images at 100× and 300× magnifications, respectively.

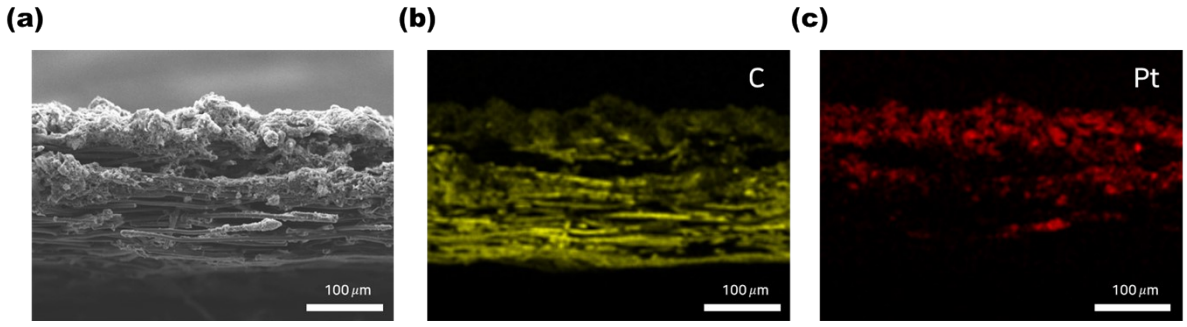

Figure S22. Cross-sectional SEM image and elemental mapping of the PVA-coated GDE after the AEMWE durability test. (a) Cross-sectional SEM image of the PVA-coated GDE after long-term operation. (b) C elemental map and (c) Pt elemental map, showing the fibrous carbon-paper substrate and the Pt-containing catalyst layer remaining localized near the top surface of the electrode.

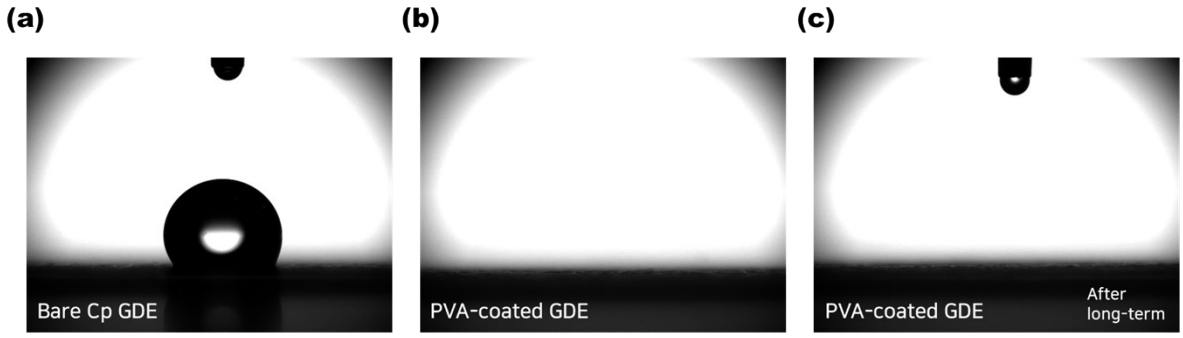

Figure S23. Wettability images of the GDEs before and after the AEMWE durability test. Images of water droplets on the (a) bare CP GDE, (b) fresh PVA-coated GDE, and (c) PVA-coated GDE after long-term operation, showing that the PVA-coated GDE remains markedly more hydrophilic than the bare CP GDE even after the durability test.

Note S1.

On an ideal, flat, chemically homogeneous surface, a water droplet in air and an air bubble in water probe the same three-phase equilibrium, so their contact angles are supplementary ($\theta_b + \theta_w = 180°$) where θ_w is the water-in-air contact angle and θ_b is the bubble-in-water contact angle. (Young's law) Accordingly, wettability reverses between the two environments: hydrophilicity in air corresponds to aerophobicity in water, and hydrophobicity in air to aerophilicity in water. [**ref:** *AIP Advances*, 2024, 14, 10, 105023, *Nature Communications* 2018, 9, 4185, *Frontiers in Chemistry* 2020, 8, 828]

S = Solid, L = Liquid, V = Vapor

W = Water, A = Air , B = Bubble

$\gamma_{SA} - \gamma_{SW} = \gamma_{AW} cos\theta_w$

$\gamma_{SW} - \gamma_{SA} = \gamma_{AW} cos\theta_b$

$cos\theta_b = - cos\theta_w$, $\theta_b + \theta_w = 180°$

However, the carbon paper used as the gas-diffusion electrode in this study is rough, porous, and chemically heterogeneous. Consequently, the measured contact angles are apparent rather than Young's intrinsic angles. As they depend on the wetting state (e.g., Wenzel or Cassie–Baxter), the simple equation $\theta_b + \theta_w = 180^\circ$ generally does not hold on such substrates. [**ref:** *Annual Review of Materials Research* 2008. 38, 71-99] Nevertheless, the inverse relation is maintained: as the water-in-air contact angle θ_w decreases (greater hydrophilicity), the bubble-in-water contact angle θ_b tend to increase (greater aerophobicity), and vice versa.

Due to the inverse relation between hydrophilicity and aerophilicity, creating "hydrophilic yet aerophilic" or "hydrophobic yet aerophobic" surface typically requires advanced surface engineering that decouples the two state (e.g. micro/nano-patterning [**ref**: Langmuir 2022, 38, 3276–3283], re-entrant textures [**ref**: Advanced Materials Technologies 2023, 8, 2201836], or chemically heterogeneous (biphilic/Janus) designs) [**ref**: *Science Advances* 2023, 9, eadd6978] [**ref**: ACS Applied Materials & Interfaces 2020, 12, 23627–23634], rather than simply changing the polymer alone. [**ref**: Frontiers in Chemistry 2020. 8, 828] Such approaches are beyond the scope of the present work, which targets simple, low-cost, and scalable coating for GDEs.

Note S2.

Classical nucleation theory (CNT) provides the fundamental framework for understanding bubble formation and is the most widely used to explain the nucleation process. CNT describes the nucleation rate in terms of the activation barrier that must be overcome for the creation of a new nucleus. This barrier corresponds to the change in Gibbs free energy, ΔG, the combined thermodynamic and kinetic activation potential.

The total free energy change (ΔG_{hom}) can be expressed as the sum of two opposing contributions: the surface energy term (ΔG_{surf}) increases with the creation of a new interface, and the volume free energy term (ΔG_{vol}) decreases as the vapor phase forms within the liquid. The competition between these two terms determines the overall energy barrier for nucleation. Consequently, the free energy of homogeneous nucleation can be expressed as a function of the bubble radius, R, to evaluate the critical size at which a stable nucleus can form.

$$\Delta G_{hom} = 4\pi\sigma R^2 - (\frac{4\pi}{3})\Delta g_v R^3$$

σ (N/m) is the surface tension between the liquid electrolyte and the gas bubble and Δg_v (J/m³) indicates the energy density difference between the dissolved and gaseous states of the molecules inside the bubble. In the above equation, the term $4\pi\sigma R^2$ corresponds to ΔG_{surf} and has a positive contribution because additional energy is required to create a new interface. The term $(\frac{4\pi}{3})\Delta g_v R^3$ corresponds to ΔG_{vol} and has a negative contribution because an increase in volume leads to a more energetically stable state.

Heterogeneous nucleation can be described by introducing a geometric factor $f(\theta_b)$ that accounts for the bubble contact angle (θ_b). The heterogeneous nucleation free energy can be expressed as $\Delta G_{het} = f(\theta_b)\,\Delta G_{hom}$, and the geometric factor is defined as $f(\theta_b) = \frac{1}{4}(2 + \cos\theta_b)(1 - \cos\theta_b)^2$. This geometric factor modifies the nucleation energy barrier (ΔG*), which determines how easily a new phase can form at the surface. Bubble nucleation predominantly occurs on the electrode surface, and the surface characteristics strongly influence the nucleation behavior. When the surface is aerophobic and hydrophilic, the bubble contact angle becomes large, leading to a higher energy barrier and making nucleation less favorable. In contrast, aerophilic and hydrophobic surfaces exhibit a smaller bubble contact angle, which lowers the energy barrier and facilitates nucleation. In this study, the catalyst was coated onto the carbon paper gas diffusion layer (GDL) to fabricate the electrode. The prepared electrode was used in the form of a gas diffusion electrode (GDE). The surface wettability of the electrode changes depending on the concentration of the PVA coating solution, and this variation has a significant effect on the bubble nucleation and growth behavior. The energy barrier for heterogeneous nucleation can also be expressed as a function of overpotential (η). [**ref**: Journal of The Electrochemical Society 2018, 165, E694]

$$\Delta G^*_{Het} = f(\theta b)\frac{16\pi\sigma^3 V^2}{3(zF\eta)^2}$$

Here, σ represents the surface tension at the liquid/gas interface, V is the specific volume of the nucleating bubble, z is the transferred ion charge, and F is Faraday's constant.

Note S3.

The bubble departure diameter can be calculated by the Fritz correlation. This equation is derived from the balance between the buoyant force(F_b) and the surface tension force(F_s) acting on the bubble. The effects of acceleration and inertia forces are considered negligible. The main forces acting on the bubble are the buoyant force acting upward and the vertical component of the surface tension that holds the bubble on the surface. The moment of bubble departure occurs when these two forces become balanced.

The buoyant force is determined by the density difference between the liquid and gas phase and the gravitational acceleration, which gives

$$F_b = V_b(\rho_l - \rho_g)g$$

Meanwhile the vertical component of the surface tension that fixes the bubble on the surface can be expressed as

$$F_s = \sigma(\pi D)sin\varphi$$

Where σ is the surface tension and φ is the contact angle at the liquid-solid interface and D is the bubble diameter.

At the moment of detachment, so by equating the buoyant force and the surface force, the classic Fritz correlation (D_d=$0.0208^{\varphi\{\sigma/[g(\rho_l - \rho_g)]\}})^{1/2}$ for the bubble departure diameter can be obtained.

Note S4

To clarify how bubble behavior influences the ohmic loss, the bubble-induced resistance was examined from three complementary perspectives: the effective electrolyte conductivity at the GDE, the projected bubble coverage estimated from the bubble detachment diameter, and the accessibility of macroporous gas-release pathways inside the porous network.

The effective electrolyte conductivity is expressed as

$$\kappa\_\mathrm{eff} = \kappa_0(1-\emptyset)^{1.5}$$

When bubbles block the electrolyte-filled pathway on the GDE, that is, when the bubble coverage $\emptyset$ increases, κeff decreases, thereby increasing the ohmic overpotential.

To quantitatively explain this, we first calculated the bubble detachment diameter using the Fritz correlation. The calculated bubble detachment diameter was approximately 4.8 mm for Bare CP, while those for PVA-C0.25 and PVA-C4 were approximately 2.9 mm and 2.5 mm, respectively. Assuming that the bubble coverage is proportional to the square of the bubble detachment diameter, D_b^2, the bubble coverage ratio between PVA-C0.25 and Bare CP can be calculated as follows:

$$\frac{\emptyset_{bub,\,PVA-0.25}}{\emptyset_{bub,\,Bare\,CP}} \propto \left(\frac{D_{b,\,PVA-C0.25}}{D_{b,\,Bare\,CP}}\right)^2 = \left(\frac{2.9}{4.8}\right)^2 = 0.373$$

The calculated result indicates that PVA-C0.25 can reduce the projected electrode coverage area of an individual bubble by approximately 63% compared with Bare CP. In addition, since an increase in the bubble contact angle induced by PVA coating decreases the bubble detachment diameter, the reduction in bubble coverage during operation can be attributed, at least in part, to the decrease in the individual bubble coverage.

However, for PVA-C4, the calculated bubble detachment diameter was similar to, or even slightly smaller than, that of PVA-C0.25. Therefore, if only surface aerophobicity and bubble detachment diameter are considered, PVA-C4 should also exhibit a similarly low level of bubble-induced ohmic resistance as PVA-C0.25. However, the EIS results showed an increase in the ohmic resistance of PVA-C4. This indicates that changes in the pore structure inside the GDL, particularly the loss of macropore pathways responsible for bubble removal, should also be considered to explain the performance degradation of PVA-C4. To examine this, the mercury intrusion porosimetry was conducted (**Table S4, Figure S19**).

Since the median pore diameter was approximately 26–28 μm, macropores were assumed to be pores larger than 25 μm. Based on this definition, the loss of gas-release pathways was quantified by integrating the log differential intrusion curve, as shown below.

$$V_{macro} = \int_{log\,25\mu m}^{log\,D_{max}} \frac{dV}{dlogD} dlogD$$

$$f = \frac{V_{macro}}{Total\ Intrusion\ Volume}$$

By integrating the curve over the pore size range above 25 μm, the macropore volume and macropore volume fraction were estimated to be approximately 1.488 mL/g and 62.3% for Bare

CP, respectively. For PVA-C0.25, these values were approximately 1.367 mL/g and 64.9%, while for PVA-C4 they were approximately 0.984 mL/g and 55.0%. These results indicate that PVA-C0.25 does not show a significant change in macropore volume fraction compared with Bare CP. However, as the concentration of the PVA coating solution becomes excessive, the macropore volume decreases in PVA-C4.

In addition, from the perspective of bubble transport, a low capillary entry pressure barrier is also required for bubbles to pass through the porous GDL. As the pore radius increases, the capillary barrier that bubbles must overcome to pass through the pore throat becomes smaller. To compare this effect relatively, the capillary barrier can be approximated as follows:

$$P_c \propto \frac{|cos\theta_b|}{r_{pore}}$$

Here, r_{pore} was assumed to be the median pore radius obtained from MIP. This equation is used as an indicator for comparing the relative bubble-removal barrier between PVA-C0.25 and PVA-C4, rather than for calculating the absolute pressure value. In PVA-C4, the pore radius decreases, and the increased bubble contact angle raises the capillary barrier. As a result, bubble removal becomes more difficult than in PVA-C0.25. Therefore, while the additional improvement in surface aerophobicity is limited, the increase in the capillary barrier caused by pore narrowing acts to hinder bubble removal and may increase the bubble residence time.

Note S5

When the additional ohmic voltage loss induced by the reduced electronic conductivity of the coating layer was estimated using the experimentally measured conductivity values for each PVA concentration, its contribution was found to be on the order of 10^{-5} V. This value is far too small to explain the difference in ohmic loss measured by EIS. Therefore, the performance degradation of PVA-C4 cannot be attributed solely to an increase in electronic resistance. Although the electronic conductivity decreases with increasing PVA concentration, its relative contribution to the observed ohmic-loss increase is limited.

Ohmic resistance is generally expressed as follows:

$$R = \frac{L}{\kappa_{eff} * A}$$

Table S1. Areal mass loading of PVA retained on CP substrates after dip-coating, rinsing, and drying, determined gravimetrically from the sample weight difference before and after coating.

Sample	PVA-C4	PVA-C2	PVA-C1	PVA-C0.5	PVA-C0.25	PVA-C0.1	PVA-C0.05	PVA-C0.025
Areal mass loading (mg cm^{-2})	1.81	1.42	0.56	0.15	0.07	0.04	0.02	0.01

Table S2. Comparison of charge density and collection efficiency (defined as Tip HOR charge density / Substrate HER charge density * 100%) of bare CP GDE and PVA coated GDE.

	Bare CP GDE						PVA coated GDE					
	(0, -1500, 0)		(0, -3000, 0)		(0, -4500, 0)		(0, -1500, 0)		(0, -3000, 0)		(0, -4500, 0)	
	Q ($C\ cm^{-2}$)	CE (%)	Q ($C\ cm^{-2}$)	CE (%)	Q ($C\ cm^{-2}$)	CE (%)	Q ($C\ cm^{-2}$)	CE (%)	Q ($C\ cm^{-2}$)	CE (%)	Q ($C\ cm^{-2}$)	CE (%)
-50 mA cm^2	0.18	1.80	0.34	3.40	0.37	3.70	0.19	1.90	0.18	1.80	0.24	2.40
-200 mA cm^2	0.26	0.64	0.30	0.75	0.66	1.65	0.12	0.30	0.18	0.40	0.30	0.75

Table S3. Comparison of current fluctuation amplitudes at the UME due to gas bubble collisions during HER of bare CP GDE and PVA coated GDE.

	Bare CP GDE			PVA coated GDE		
	(0, -1500, 0) (nA)	(0, -3000, 0) (nA)	(0, -4500, 0) (nA)	(0, -1500, 0) (nA)	(0, -3000, 0) (nA)	(0, -4500, 0) (nA)
-50 mA cm^{-2}	1.41 ± 1.08	3.82 ± 1.31	17.88 ± 12.83	0.63 ± 0.47	0.94 ± 0.55	1.62 ± 0.68
-200 mA cm^{-2}	2.40 ± 2.70	2.26 ± 1.60	45.68 ± 11.88	1.03 ± 0.86	1.06 ± 0.42	2.79 ± 7.77

Table S4. Pore structure parameters of bare CP, PVA-C0.25, and PVA-C4 determined by Mercury Intrusion Porosimetry (MIP).

Sample	Total Intrusion Volume (mL g^{-1})	Median Pore Diameter (μm)
Bare CP	2.387	28.55
PVA-C0.25	2.106	28.45
PVA-C4	1.791	26.05

Table S5. Comparison of representative bubble-management strategies reported for AEMWE and closely related water-electrolysis systems.

Refs.	Electrode/Substrate	Fabrication	System (condition)	Performance	Durability
[1]	Nanostructured MoS_2 film / Ti foil	Hydrothermal synthesis	Half-cell, HER (0.5 M H_2SO_4)	170 mA cm^{-2} at −0.5 V vs. RHE	Over 350 minutes at 170 mA cm^{-2}
[2]	Ni nanorod arrays (Ni-80) / Ti foil	Oblique angle deposition	Half-cell, HER (1.0 M KOH)	271 mV at 100 mA cm^{-2}	36 h at 10 and 50 mA cm^{-2}
[3]	Monolayer NiFe-LDH / Ni foam	Coprecipitation with formamide	Full cell, AEMWE (1 M KOH, 50°C)	1.69 V at 1 A cm^{-2}	50 h at 1 A cm^{-2}
[4]	NiFe based catalyst / Hierarchical 3D-printed Ni GDL	Direct ink writing 3D printing	Full cell, AEMWE (pure water, 80°C)	2.0 A cm^{-2} at 1.95 V	50 h at 200 mA cm^{-2}
[5]	Polyethyleneimine hydrogel-coated Ni foam	Dip-coating, Schiff-base crosslinking with glutaraldehyde, freeze, drying	Half-cell, HER (1.0 M KOH)	488.6 mA cm^{-2} at −0.6 V vs. RHE	20 h at 500 mA cm^{-2}
[6]	M13 viral hydrogel-coated Pt film / FTO	E-beam Pt deposition, APTES surface modification, glutaraldehyde cross-linking of M13 virus hydrogel	Half-cell, HER (0.5 M H_2SO_4)	146 mV at 10 mA cm^{-2}	30 h at -0.25 V vs. RHE
[7]	Sn_4P_3/Co_2P “stalk”-“cap”-typed nanoarrays / Ni foam	Hydrothermal growth, 2-methylimidazole-assisted self-assembly / ion exchange, phosphorization	Two-electrode overall water splitting (1 M KOH)	1.56 V at 10 mA cm^{-2}	100 h at 10 and 200 mA cm^{-2}
This work	PVA-coated carbon paper (PVA-C0.25) with Pt/C catalyst	Dip-coating	Full cell, AEMWE (1 M KOH, 50°C)	2.85 A cm^{-2} at 2.0 V	>100 h at 1 A cm^{-2}

1. Z. Lu, W. Zhu, X. Yu, H. Zhang, Y. Li, X. Sun, X. Wang, H. Wang, J. Wang and J. Luo, Advanced Materials, 2014, 26, 2683-2687.
2. J. Kim, S. M. Jung, N. Lee, K. S. Kim, Y. T. Kim and J. K. Kim, Advanced Materials, 2023, 35, 2305844.
3. S. S. Jeon, J. Lim, P. W. Kang, J. W. Lee, G. Kang and H. Lee, ACS Applied Materials & Interfaces, 2021, 13, 37179-37186.
4. B. Huang, X. Wang, W. Li, W. Tian, L. Luo, X. Sun, G. Wang, L. Zhuang and L. Xiao, Angewandte Chemie International Edition, 2023, 62, e202304230.
5. M. Bae, Y. Kang, D. W. Lee, D. Jeon and J. Ryu, Advanced Energy Materials, 2022, 12, 2201452.
6. D. Jeon, J. Park, C. Shin, H. Kim, J.-W. Jang, D. W. Lee and J. Ryu, Science Advances, 2020, 6, eaaz3944.
7. X. Qin, B. Yan, D. Kim, Z. Teng, T. Chen, J. Choi, L. Xu and Y. Piao, Applied Catalysis B: Environmental, 2022, 304, 120923.